

AD-A178 986

A COMPUTATIONAL AND EXPERIMENTAL STUDY OF HIGH-SPEED
IMPULSIVE NOISE FROM A ROTATING CYLINDER(U) ARMY
AVIATION RESEARCH AND TECHNOLOGY ACTIVITY MOFFETT FIELD
C . . T M PURCELL 1987

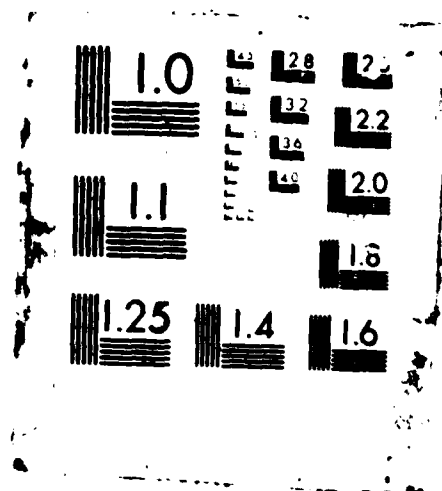
1/1

UNCLASSIFIED

F/G 28/4

NL





AIAA '87

AD-A178 986

Paper No. 87-0253

A COMPUTATIONAL AND EXPERIMENTAL STUDY OF HIGH-SPEED IMPULSIVE
NOISE FROM A ROTATING CYLINDER

T. W. Purcell

Aeroflightdynamics Directorate
US Army Aviation Research and Technology Activity
Ames Research Center
Moffett Field, CA 94035-1099

DTIC
ELECTE
APR 07 1987
S D

DISTRIBUTION STATEMENT A

Approved for public release;
Distribution Unlimited

AIAA 25th
AEROSPACE SCIENCES MEETING
January 12-15, 1987/Reno, Nevada

DISCLAIMER NOTICE

**THIS DOCUMENT IS BEST QUALITY
PRACTICABLE. THE COPY FURNISHED
TO DTIC CONTAINED A SIGNIFICANT
NUMBER OF PAGES WHICH DO NOT
REPRODUCE LEGIBLY.**

A COMPUTATIONAL AND EXPERIMENTAL STUDY OF HIGH-SPEED IMPULSIVE NOISE FROM A ROTATING CYLINDER

T. W. Purcell*

Aeroflightdynamics Directorate
US Army Aviation Research and Technology Activity
Ames Research Center
Moffett Field, CA 94035-1099

Abstract

This work presents an alternative to current integral approaches that do not accurately predict noise from a delocalized rotor. The two-dimensional model of this study is essentially an airfoil shape mounted on the side of cylinder which spins at transonic speeds between two end-walls. A finite-difference conservative formulation of the two-dimensional, transonic full-potential equations solves the flow field away from the body directly and hence predicts the beginning of delocalization and the associated wave propagation. The potential method has an inherent stability limit at a free-stream velocity of Mach 1.4 and shows a troubling sensitivity to the choice of outer boundary conditions. Methods for correctly handling these two problems are shown. A two-dimensional experiment that simulates the conditions assumed by the computer code is described. The computer prediction of the flow expected in the experiment is presented as are some limited experimental results. Results taken from a three-dimensional hovering rotor code show how the current two-dimensional results correlate to those from an actual rotor. Results for low-aspect-ratio rotors show a higher delocalization Mach number for decreasing aspect ratio and a greater dependence on thickness.

Introduction

High-speed impulsive (HSI) noise is emanated when a transonic rotor creates such a strong shock that the shock leaves the blade and propagates into the free-stream. This free-stream shock, or delocalized shock, creates several problems for integral methods. Earlier research has been applied to this problem but with little success.¹⁻³ More recent works have fared better⁴⁻⁸ with this "delocalization" problem, as Caradonna and Leom⁵ termed this spreading of the shock. Photographs of such delocalized shocks radiating from model propellers were produced by Hilton¹⁰ in 1938 and more recently by Tangler¹¹ in 1977 for a model helicopter rotor in a forward flight condition. A similar phenomenon is seen in hovering helicopter rotor tests at high tip-Mach-numbers. Hot-wire studies from Schmits and Yu¹² experimentally demonstrate the extent of the supersonic zones relative to the rotor on and around the tip. Figure 1 shows results from their study along with the associated changes in sound signatures as the tip-shock delocalizes. These results are from a hovering rotor model with a NACA 0012 airfoil and aspect ratio of 13.7.

One of the most familiar integral formulations for solving acoustics problems was presented by Ffowcs-Williams and Hawkings:¹³

$$4\pi a_0^2 \rho'(\vec{x}, t) = \frac{\partial}{\partial t} \iint \left(\frac{\rho_0 v_n}{r|1-M_r|} \right) dS(\vec{\eta}) - \frac{\partial}{\partial x_i} \iint \left(\frac{P_{ij} n_j}{r|1-M_r|} \right) dS(\vec{\eta}) + \frac{\partial^2}{\partial x_i \partial x_j} \iiint_V \left(\frac{T_{ij}}{r|1-M_r|} \right) dV(\vec{\eta}) \quad (1)$$

*Research Scientist. Member AIAA.

This paper is declared a work of the U.S. Government and therefore is in the public domain.

Applications using the linear terms of this equation work well except when a large shock appears in the flow.¹⁴ Even using the full nonlinear portion of the Ffowcs-Williams and Hawkings (FWH) equation gives incorrect trends when a rotor has a delocalized tip shock.¹⁵ Schmits and Yu¹⁴ use the first, or monopole, term of the FWH equation in their linear analysis of a hovering rotor. This dipole term has almost no effect on the predicted pressure pulse when compared with the monopole or thickness term prediction.^{14,15} The third and last term of the FWH equation is the quadrupole term, which has no simple physical analogue like the other two terms. Quadrupole terms describe the fluid distortions and pressures over a volume near the blade tip and are quite necessary to accurate tracking of a disturbance as it moves off the blade. This last term is extremely difficult to integrate or model, but its inclusion has been shown to improve the pulse predictions significantly. Yu et al.¹⁶ completed a complex nonlinear quadrupole solution that greatly improves the solutions but still has difficulty with delocalized cases.¹⁷ Perhaps a differential method would work better in such cases.

There are several three-dimensional codes that model the transonic rotor-tip flow field using finite-difference (FD) formulations,^{18,19} but these codes only predict the flow near the rotor tip and tend to damp any waves that spread off the blade surface. Kirchhoff methods map a linear pressure wave to some other physical point²⁰ when provided with an accurate starting wave. However, there is no direct way to connect the surface-pressure solution with the pressure field off the blade.

There has been one research effort that couples a two-dimensional FD solution near some arbitrary disturbance to an acoustic-wave solver away from the blade. Rutherford²¹ presented a small-disturbance, nonconservative, two-dimensional shock-fitting potential code for the innermost portion and a MacCormack solution of the discretized wave equation which uses initial boundary conditions defined by the potential code.

The work presented here develops experimental and numerical techniques for the direct prediction of noise propagation from a two-dimensional rotating cylinder with a potential FD method. This two-dimensional approach allows investigation of such problems as stability limits and the selection of proper boundary conditions, problems that arise in potential codes used in supersonic zones.

Previous studies by Schmits and Yu,¹⁵ which show that only the last 10% of a blade determines most of the HSI noise levels and that lift has little effect, indicate the acceptability of the two-dimensional approach. Figure 2 shows how the two-dimensional cylinder model correlates to a generic rotor blade. Such a two-dimensional experiment is described and conducted to verify the simplified model and computer code. Figure 3 is a sketch of this physical test. Boundary-layer problems found while running the tests mandated a correction to the inviscid computer code. Limited results from this experiment and the computer solutions are presented to validate the code and to form a basis for extrapolations to real helicopter problems. Some surprising trends appear in the predicted results for the



Dist	
A-1	

short rotors typical of a propeller or tilt-rotor-type application.

Governing Equations

The usual unsteady continuity and density equations in cylindrical coordinates provide the basis for the finite-difference code of this work. After transformation to a rotating coordinate system, a computational variables transformation²² yields the following nondimensional equations for programming:

$$(\rho U)_\theta + (\rho V)_r = 0 \quad (2)$$

$$\rho = [1 - \frac{\gamma-1}{2} M_c^2 (U^2 + V^2 - U_\infty^2)]^{\frac{1}{\gamma-1}} \quad (3)$$

where the velocities U , U_∞ , and V are defined as $(Y + \frac{1}{2}\phi_\theta)$, Y , and $(Y\phi_r)$, respectively, and where ρ is the fluid density, γ is the ratio of specific heats, a is the free-stream speed of sound, ϕ is the usual flow potential, r is the radial dimension and distance, and θ is the circumferential dimension.

The density ρ and the velocity components $\frac{1}{2}\phi_\theta$ and ϕ_r are nondimensionalized by ambient density and by the cylinder surface velocity, ΩR , respectively, where Ω is the angular velocity and R is the radius of the cylinder. The radial distance r is nondimensionalized by chord length c ; the circumferential variable θ is nondimensionalized by the sector width occupied by the airfoil on the cylinder edge. This sector width is also given by the inverse of the aspect ratio, AR , which is similar to the aspect ratio of a rotor blade and is defined as R/c in previously defined variables. An additional factor, Y , is introduced to convert the scale of the radial distance variable to cylinder radii lengths. This factor Y is defined as r/R , which appears as the radial distance in the equations below. Finally, $M_c = \Omega R/a$ is the cylinder Mach number.

Further transformations for computational considerations follow conventional procedures for conservation forms:^{23,24}

$$\left(\frac{\rho U}{J}\right)_\xi + \left(\frac{\rho V}{J}\right)_\eta = 0 \quad (4)$$

$$\rho = \left[1 - \frac{\gamma-1}{2} \frac{M_c^2}{Y} (A\phi_\xi^2 + 2B\phi_\xi\phi_\eta + C\phi_\eta^2)\right]^{\frac{1}{\gamma-1}} \quad (5)$$

The quantities U and V , called the contravariant velocity components along the ξ and η directions, respectively, are defined below. Metrics A , B , C , D , and E and the Jacobian, J , are groups of various mapping quantities that arise during transformation; they are defined as

$$\begin{aligned} A &= \frac{1}{Y} \xi_\theta^2 + Y \xi_r^2 \\ B &= \frac{1}{Y} \xi_\theta \eta_\theta + Y \xi_r \eta_r \\ C &= \frac{1}{Y} \eta_\theta^2 + Y \eta_r^2 \\ D &= \xi_\theta Y \\ E &= \eta_\theta Y \\ J &= \xi_\theta \eta_r - \xi_r \eta_\theta \end{aligned} \quad (6)$$

Numerical Solution

A successive-line over-relaxation (SLOR) method solves the differenced equations outlined below. An artificial density scheme builds in proper zones of dependence and allows the use of simple central-difference operators in all regions. Second-order-accurate formulas determine the

flux terms ρU and ρV at midpoint locations. The continuity equation is differenced to make the total operator centrally differenced about a node point:

$$\delta \left(\frac{\rho U}{J} \right) + \delta \left(\frac{\rho V}{J} \right) = 0 \quad (7)$$

where δ indicates a central-difference operator. The U and V terms are the velocities described previously and are found as shown:

$$U_{j+1/2,k} = (A\phi_\xi + B\phi_\eta + D)_{j+1/2,k}$$

$$V_{j,k+1/2} = (B\phi_\xi + C\phi_\eta + E)_{j,k+1/2}$$

where the A , B , C , D , and E metrics are found at the node points, using standard second-order-accurate finite-difference operators. All metrics quantities are found and stored at node points (j,k) , and simple averages are used for values away from grid nodes.

The density values used in the continuity equation, $\bar{\rho}_{j+1/2,k}$ and $\bar{\rho}_{j,k+1/2}$, are defined as

$$\bar{\rho}_{j+1/2,k} = [(1-\nu)\rho]_{j+1/2,k} + \nu_{j+1/2,k} \rho_{j+1+1/2,k} \quad (8)$$

$$\bar{\rho}_{j,k+1/2} = [(1-\nu)\rho]_{j,k+1/2} + \nu_{j,k+1/2} \rho_{j,k+m+1/2}$$

where

$$l = \pm 1 \text{ when } U_{j+1/2,k} \lesseqgtr 0 \quad (9)$$

$$m = \pm 1 \text{ when } V_{j,k+1/2} \lesseqgtr 0$$

Density is found after a sweep of the flow field has updated all the ϕ values from the nondimensional equation

$$\rho = [1 - 0.2M_c^2 (U^2 + V^2 - Y^2)]^{2.5} \quad (10)$$

where M_c is the Mach number of the cylinder surface. Borrowing from finite-volume techniques, the densities are found at cell-centered locations $(j+1/2, k+1/2)$, which are then averaged appropriately to yield the needed values at $(j+1/2, k)$ and at $(j, k+1/2)$. This technique has been shown by South in Hafez et al.²⁵ to yield a more compact calculation cell for density. The cell-centered values require ϕ derivatives found separately from the derivatives used in the continuity equation.

The switching function ν determines when to start using an upstream density value and is hence controlled by Mach number. Control for ν in the ξ -direction is given by

$$\nu_{j+1/2,k} = \max[0, 1 - 1/M_{j,k}^2] \text{ for } U_{j+1/2,k} > 0 \quad (11)$$

and

$$\nu_{j+1/2,k} = \max[0, 1 - 1/M_{j+1,k}^2] \text{ for } U_{j+1/2,k} < 0 \quad (12)$$

Control in the vertical direction, or η -direction, is given similarly.

A SLOR technique solves the linearized continuity equation. Linearization comes from simply lagging the density one iteration step so that for each iteration, density is considered constant and is updated after each horizontal sweep of the flow field.

Steger and Caradonna²⁶ show an alternative to the standard switched schemes which proves stable in almost all regimes:

$$\Delta_\eta \nabla_\eta \phi - M^2 \nabla_\eta \nabla_\eta \phi + \Delta_\eta \nabla_\eta \phi = 0 \quad (13)$$

In this and subsequent sections the ∇_η and Δ_η symbols represent backward and forward difference operators, respectively, with the subscript denoting direction. Combinations of these two symbols show higher derivatives such as the second-order differences: $\nabla_\eta \nabla_\eta$ for a backward difference or $\Delta_\eta \nabla_\eta$ for a central difference. Fortunately this mix of differencing operators closely corresponds to the artificial density method and permits an easy analysis of stability,

as will be shown briefly. Details of this correspondence are explained in the paper by Steger and Caradonna.²⁶

Stability Analysis of the Solution Scheme

A stability analysis of any finite-difference method comes from the Von Neumann linear stability analysis (LSA). Solving for the amplification factor results in the following expression, whose magnitude must be less than one for stability:

$$\begin{aligned} & \{ \cos(\alpha) + i[\sin(\alpha)] / \\ & \{ 2 - \cos\alpha + M^2(1 + \cos 2\alpha - 2\cos\alpha) + \\ & \frac{4}{\gamma} \sin^2 \frac{\beta}{2} + \\ & i[\sin\alpha + M^2(2\sin\alpha - \sin 2\alpha)] \} \end{aligned} \quad (14)$$

where γ is the computational cell aspect ratio $(\Delta y / \Delta x)^2$, and α and β are the wave numbers for the x - and y -directions, respectively.

The usual error-amplification portraits are shown in Fig. 4 for the undamped and damped cases. As Mach number increases, an associated increase in amplitude for lower wave numbers (low-frequency errors) is seen. The stability limit at Mach 1.4 is seen by the flat line, showing unity gain for errors with wave numbers near zero. Any higher speeds will quickly go unstable as shown in the curve from the Mach 2.0 case.

A damping term added to the iteration or correction matrix allows stable solutions with higher Mach numbers. This damping term also increases the diagonal dominance of the correction matrix; it simply adds a spatial operator to the correction term in the general relaxation equation below:

$$(N + D\nabla_x)C^n + \omega L\phi^n = 0 \quad (15)$$

where C^n is the correction $(\phi^{n+1} - \phi^n)$; $L\phi^n$ is the residual, which indicates how well the finite-difference equations have converged; and ω is the overrelaxation control, which is usually set within the range 1.9 - 2.0. The D coefficient controls the amount of damping added to the solution. This approach will not change the solution since the correction term goes to zero as the solution converges. Only the path of the convergence changes, so that stability is maintained. Hence, a new time-path is taken if the iteration levels are considered time-levels. This variation may have serious implications for time-accurate codes.

Parametric studies of this damping D show that it must increase as $M^{3/2}$ to maintain stable iterations. For the cases shown, at Mach numbers of 2.0 and 4.0, damping coefficients of -1 and -4, respectively, maintain stability. The damping effect pulls the amplification factor curve to the unity line in areas where it was previously very high.

Grid Generation

A sheared "H" grid, similar to grids usually used for nonlifting airfoil studies, is used here for all rectilinear motion cases. The cylindrical motion cases require a more sophisticated grid concentration in regions where the shock pulse is expected to move into the flow field. The following Poisson-like equation specifies grid concentration in one direction only:

$$r_{\eta\eta} = C F(\theta) r$$

The C factor determines how much the grid clusters to the control function, $F(\theta)$. The control function varies in the θ -direction, so that the grid clusters to any curve. This curve usually comes from the linear characteristic line so that grid cells cluster to the region where information from the airfoil travels. The radial lines are specified separately. This non-orthogonal clustering to a general line imparts a skewing of the grid cells that creates convergence and

stability problems for the solution algorithm. Hence, only a weak clustering is used.

Boundary Conditions

Flow tangency at the body surface is enforced by

$$\phi_{\eta}|_{body} = \left(\frac{-Y\eta_{\theta}}{J C} - \frac{B}{C} \phi_{\xi} \right) |_{body}$$

The far boundary conditions specify nonreflection conditions in a manner similar to those used in airfoil codes.²⁷ The general potential equation is solved at the outer boundary instead of the usual arbitrary and, hence, wrong boundary condition of setting ϕ to zero. This nonreflection approach solves an approximation shown below to the potential equation:

$$\hat{U} \frac{1}{Y} \phi_{\theta} + \hat{V} \phi_r = 0 \quad (16)$$

where \hat{U} and \hat{V} are constants found from the previous iteration; they are defined as

$$\begin{aligned} \hat{U} &= Y + \frac{1}{Y} \nabla_{\theta} \phi + U' \\ \hat{V} &= \nabla_r \phi + V' \end{aligned} \quad (17)$$

The $(\)'$ quantities change, depending on the boundary location as defined by the following:

$$\begin{aligned} U' &= 0, \quad V' = \frac{1}{M_c}; & \text{on outer boundary} \\ U' &= \frac{1}{\sqrt{2}M_c}, \quad V' = \frac{1}{\sqrt{2}M_c}; & \text{at upper rear corner point} \\ U' &= \frac{1}{M_c}, \quad V' = 0; & \text{along aft boundary} \end{aligned}$$

The upstream ϕ values are held to zero, and, of course, the change to computational variables transforms all of the above boundary-condition equations to ξ, η space.

The nonreflection boundary condition above [Eq. (16)] produces much better solutions when proper (upstream) difference operators are used as needed. This upstream differencing is sufficiently implemented by using backward-difference operators on both the vertical and horizontal derivatives and using a marching procedure toward the upper right-hand corner point.

Results

The computational code was first validated in the cartesian mode and compared with a similar code's results. The validated code was then used in the cylindrical mode to predict the experimental results. After finding differences in the experimental results and the code predictions, corrections to the code were used to modify the predicted results.

Computational Results

This code shows proper solutions when compared with other established transonic codes. Rectilinear motion results compare well with similar results published by Holst and Ballhaus²³ for Mach numbers of 0.70 and 0.84 using a circular-arc, 10%-thick airfoil. Stability limitations are a problem for potential codes like the code of this study when the flow field contains a region of high-speed flow (e.g., Mach 1.4 or greater). The previous section on stability shows how a linear model of the potential equation stabilizes at Mach numbers of 2.0 and greater for properly controlled damping. A high-Mach-number case, which is stabilized by this added damping, appears next. Figure 5 shows the surface pressures from a Mach 2.0 rectilinear

motion test. The solid line in Fig. 5 shows the expected linear results for this supersonic case as found from shock-expansion theory. The analytical and computed solutions match very well, thereby demonstrating that difficult and usually unstable cases are possible.

The results in Fig. 5 come from a high-Mach-number case to show how added damping controls an inherent instability. The same instability problems arise in the cylindrical cases when the velocity given by Ωr becomes greatly supersonic. Damping parameter levels for this Mach 2.0 case are about what are expected from the linear model case, but only near convergence. During the convergence process, the solution error starts to grow quickly, requiring an increase in the damping coefficient. Automatic damping adjustment avoids guesswork in picking a damping value. This adjustment algorithm is shown if D is taken as the damping value and superscripts indicate iteration count:

$$\begin{aligned} D^n &= 1.06 D^{n-1} \text{ if } R^n > 1.00 R^{n-1} \\ D^n &= 0.99 D^{n-1} \text{ if } R^n < 0.99 R^{n-1} \end{aligned} \quad (18)$$

The damping magnitude is usually constrained to a value of at least 0.3 but less than 25.

Complete delocalization occurs for a Mach number of 0.79 as shown in Fig. 6b by the radiating wave. Parameters for this case consist of an aspect ratio of 7, an airfoil thickness (r) of 12%, and surface Mach numbers of about 0.75. These physical parameters match those from the experimental apparatus. These results are not unlike those seen in the coarse-grid solutions. The fine-grid surface pressures seen in Fig. 6a show a finer shock width and a slightly higher negative peak than the coarse grid results. The delocalized wave seen in Fig. 6b is also resolved much better in this fine-grid case.

The shock on the surface still damps out to form a fairly smooth pulse away from the airfoil. This damping is not entirely due to a loss of resolution from grid coarseness. Grids of similar node points used on narrower domains yield a finer mesh but do not appreciably improve the final solution. A grid spacing of 20 points per chord length is believed to be sufficient. Covering the flow field out to the 16-chords location with 20 points per chord length in two directions uses almost all of the conventional memory of 2×10^6 words on the Cray XMP-4/8 at the Ames Research Center. A finer grid would require lengthy run times and special coding procedures outside the scope of this work.

Recalling that the wave equation in two-dimensions can not support a sharp discontinuity, such as a shock explains why the shock should damp out as it moves off the surface. The three-dimensional wave equation does support and propagate impulses though.²⁰ Therefore, the sharp pulses seen in hovering rotor tests are not expected in the code results or in the two-dimensional experimental results.

The wavelet that exits at the rear boundary shows how well the nonreflection conditions imposed at the outer boundaries work to accurately handle the flow near a boundary. Cases that do not have this condition, but instead use the usual procedure of simply specifying the ϕ value, produce many reflected waves at the boundaries for even simple cases. A clearly evident wave reflection appears when such arbitrary boundary conditions are applied and when the outer boundary grid is sufficiently fine to resolve the reflected wave. Another indication of incorrect boundary conditions is seen by a build-up of ϕ values in the upper right-hand corner of the solution field. This effect occurs in three dimensions also. When the nonreflection condition is disabled in another full-potential but three-dimensional code, a similar accumulation occurs at the outer boundary.²⁰ The absorption boundary condition produces remarkably improved solutions near the boundaries by eliminating both of these problems. The reflection

error is not a problem for most codes, because the grid near the outer boundaries is usually sufficiently coarse to damp out erroneous boundary reflections that might cause significant error in the surface solution, and the outer boundaries are usually placed very far from the body.

The results found from the fine-grid solution presented in Fig. 6 are reformulated to produce the results shown in Fig. 7. This presentation corresponds to the results expected from microphone data taken in terms of relative pressure during the experiment. The microphones were located 0.5, 1.0, 3.0, and 6.0 chords away from the surface.

Experimental Results

The two-dimensional experiment described here reproduces most of the conditions assumed by the computer code. A boundary-layer correction to the code allows for the viscous effects seen in the experiment. A preliminary computer simulation of this test showed that delocalized flow would occur at Mach 0.81, dictating an operating speed of 4973 rpm. Although the final simulations show delocalization at Mach 0.79, the higher speed was used in the design of the cylinder. Figure 3 shows a sketch of the basic setup of a cylinder spinning between two walls to maintain a two-dimensional flow. Pressure sensors were mounted in one support wall along a radial line from the cylinder origin, and the sensor faces were kept flush with the wall surface. The preliminary design of the cylinder was done at Ames Research Center.²¹

Figure 8 shows 1) the field pressures away from the rotating cylinder for part of a cylinder revolution and 2) how the pulse magnitude decreases with radial distance. All of the plots from experimental data come from a test in which the surface Mach number was 0.824. This velocity is well above the predicted delocalization speed yet not a hint of delocalization is seen. A pressure pulse similar to that expected from the computer code at Mach 0.79 is seen, but the magnitude is low by a factor of 5. This reduced pulse magnitude is due to the thick boundary layer observed in the test despite all efforts to reduce viscous effects through the boundary-layer removal system. Since the boundary-layer reduces the velocity of the body relative to the moving air just above the body, less of a net disturbance is created.

Figure 9 directly compares experimental pressure results at the first transducer location of 0.5 chord for a full revolution with the single pulse from the computer prediction. The observed pulse shape is about the same as expected from the pulse prediction. No strong shock is seen in either result, although the pulse is not symmetrical since it shows a sharper recovery to free-stream pressure. The smaller spike and large area of slightly positive pressure just forward of the main negative pulse in the test data comes from variations from the circular that were present in the cylinder. Clearly, the code must include both the exact cylinder shape and the boundary-layer influences.

Boundary - Layer Corrections

The approximate boundary-layer correction added to the inviscid potential code comes from an analytical solution to the Navier-Stokes equations. This correction involves modifying the Ωr component of the rotating coordinates transformation so that the no-slip condition is met at the surface and an appropriate velocity profile blends to the inviscid free-stream. The assumptions in this derivation are incompressibility, laminar and steady-state flow, and uniform suction instead of the discrete suction ports. An eddy-viscosity model takes care of the turbulence modeling.

Allowing suction and looking for a steady-state solution with $v = RV/r$ from the continuity equation, where R

is the cylinder radius and V is the uniform suction velocity at the surface, produces

$$u(r) = \Omega r \left(\frac{r}{R} \right)^{R_s} \quad (19)$$

where u is the velocity component in the θ -direction, and ν is the kinematic viscosity coefficient. The suction Reynolds number is defined as $R_s = VR/\nu$, which is negative because the suction velocity is negative, and the cylinder angular speed is given by Ω . Various tests show that the pressures can be well predicted by using $R_s = -4$. This value yields the same pressure (-1.1 lb/in.^2) that was measured in the experiment at the 0.5-chord location and produces a reasonable looking flow-velocity profile. This modified velocity introduces a minor variation from the assumed irrotational flow field, which predicts density with a negligible 5% error. However, this correction only matches the magnitude of the main pulse and fails to match to overall pulse shape seen in Fig. 9.

A detailed model of the geometric boundary conditions on the cylinder surface reflects the exact variations from circular. Pressure results using the exact geometric conditions for the cylinder are shown in Fig. 10 for a domain of a little over one-half of a revolution. The pressure results now show a great deal of similarity to measured experimental pressures (Fig. 11), except that the computed magnitudes are still high by a factor of 5. The smaller pulse after the large pulse from the airfoil bump is now well modeled, and the slowly rising positive-pressure hump observed in the test is now seen. Hence, an accurate model has been developed to predict the form of the pressures seen during the experimental testing. Now only a correction to the magnitudes is required.

This exact cylinder shape case uses the same $R_s = -4$ exponent that was previously found to produce such good matches to the observed pressures. Complete details of how the potential code includes these boundary-layer influences, as well as the exact boundary conditions of the cylinder, are given in Ref. 30. The results from such a fully corrected case are shown in Fig. 12 where they are compared with the observed experimental results for the 0.5-chord location. The boundary layer has smoothed over the sharp peaks seen in the inviscid prediction. However, the pulse magnitudes are much closer than those seen in Fig. 11. The addition of exact boundary conditions increases the main-peak magnitude, but there has been no attempt to correct this peak. Since surface details are most important in this case, a grid is used that is clustered to the body with an almost uniform grid in the circumferential direction. The computational results at points farther away from the surface show a definite loss of resolution, although the results farther out show the same trends of smeared pulses seen in the 0.5-chord plot of Fig. 12.

Design Applications

This section derives the observed two-dimensional results so that they compare with expected results from a real helicopter rotor. Figure 13 shows results from this two-dimensional code in terms of helicopter rotor nomenclature. The two-dimensional "aspect ratio" used here simply means the radius of the rotating cylinder divided by the chord length of the body attached to the cylinder's edge. This aspect ratio is similar to the usual helicopter definition of rotor radius divided by blade chord.

The general effect of various aspect ratios and thickness ratios is not surprising: to obtain a higher delocalization Mach number, simply disturb the air less. This basic principle can be achieved by using a thinner body or a large two-dimensional aspect ratio, which corresponds to a long, slender rotor blade on a real helicopter. Using thinner bodies is rather obvious since a thinner body is known to

produce a smaller disturbance. A large aspect ratio means that the relatively short body must move faster to disturb the air enough to send a disturbance off the tip to the sonic circle. Additionally, larger aspect ratios also mean there is a greater distance from the blade tip to the linear sonic circle when measured in chords. The linear sonic circle is defined as a line where the Ωr term of the rotational transformation equals the free-stream speed of sound. The distance from the cylinder edge to this sonic circle is given in chords by $R(1/M_\infty - 1)$, which increases with aspect ratio for a given cylinder surface Mach number M_∞ . A larger aspect ratio requires a larger disturbance to bridge the increased gap.

Figure 13 shows a consistent dependence on aspect ratio for most airfoil thicknesses. The body thicknesses typical of most helicopter blades produce curves that are almost parallel. The very thin bodies—3% and less—show a lack of dependence on aspect ratio. Since the edge perturbation is so small, connection to the sonic circle requires a very high Mach number. This high Mach number throws disturbances off the body that quickly develop into Mach waves, a result of nonlinear acoustic velocity effects. These Mach waves connect to the sonic circle to delocalize the flow. Since delocalization comes from such a Mach wave, the distance in chords is irrelevant. Small disturbances of various lengths produce almost identical waves. With this loss of chord-length dependence, the distances in rotor radii become important. These radii distances are given as a function of cylinder Mach number: $\frac{1}{M_\infty} - 1$. The delocalization Mach number now depends only on this distance and hence on cylinder Mach number, which explains the almost flat curve as aspect ratio changes for very thin bodies.

Since the above approach is strictly two-dimensional, tip effects are not included. A comparison with three-dimensional results reveals when tip effects are important and what effects the tip relief will have. There are very few test data available on delocalization Mach number for a broad range of rotor parameters. Hence, a small-disturbance rotor code supplies a three-dimensional data base in the place of experimental evidence.³¹ Figure 14 shows the results from this three-dimensional code for a set of parameters similar to those that are reflected in Fig. 13. Both of the studies mentioned in this section use a symmetric parabolic-arc airfoil section. The full rotor prediction shows very similar trends to those from the two-dimensional approach seen in Fig. 13. The results for the thicker blade show a smooth dependence on blade thickness and aspect ratio. The average Mach number is higher for the three-dimensional case, but the thicker blades show the same convex curve. As the blade gets thinner, the same flattening of the curve is seen. The 6%-thick blade result is slightly concave so that the delocalization Mach number actually increases for smaller aspect ratios. The two-dimensional results do not show this effect until blades that are thinner than 2% are used.

The tip relief in the three-dimensional cases explains both the higher overall delocalization Mach number and the delay in curve shape reversal. The extra dimension present in the full rotor cases allows extra room for disturbances to dissipate. Hence, a higher Mach number is required in the three-dimensional cases to achieve a disturbance strong enough to delocalize the flow. Since higher delocalization Mach numbers appear overall, the Mach wave delocalization discussed above becomes important for the thicker blade results, such as the 6% one which is concave. Again the change in curve shape occurs at Mach numbers of 0.9.

Conclusions

Techniques were developed for application to potential-flow computational fluid dynamics methods for predicting

acoustic waves. Using the potential-flow equation to define the outer boundary values for the potential, ϕ , alleviates one problem of reflected waves. A stability limit problem occurs at Mach numbers above 1.4, but adding a damping factor to the relaxation equation allows higher speeds. This damping factor comes from a linear equation analysis, and a demonstration of how it controls divergence was presented.

The computational results show a definite change in the flow field when delocalization occurs. The pressures found away from the spinning body do not show the shock-like waveform seen in hovering model-rotor tests, since a two-dimensional wave solution tends to damp discontinuities as opposed to the three-dimensional solution which preserves spikes in pressure.

A two-dimensional experiment was conducted, and limited experimental results were presented to support the findings of the computer prediction. A set of computer-code corrections for the exact cylinder shape and the boundary-layer entrainment produces results similar to those seen in the experiment.

Parametric variations with the two-dimensional computer code show a smooth dependence on airfoil thickness and aspect ratio for configurations similar to actual helicopter rotors. An unusual lack of aspect-ratio influence occurs for very thin airfoil sections (e.g., 2% and less) for which thinner disturbances create delocalization just by starting a Mach wave that is independent of chord length and, hence, aspect ratio (radius/chord).

Higher delocalization speeds overall are seen in the three-dimensional rotor code owing to tip-relief effects, which reduce any tip disturbance and thereby require a higher speed to delocalize the flow. The reversal of dependence on aspect ratio occurs for thicker blades in the rotor case but for about the same Mach number as the two-dimensional model case. This indicates that at such a high speed, Mach waves are sufficient to delocalize the flow.

The model results and the rotor results show a clear correlation. The region where tip-relief effects are important is shown and the two-dimensional model is shown to predict the expected delocalization Mach number for a real helicopter rotor based on the three-dimensional rotor code correlations.

References

- ¹ Deming, A. F., "Noise from Propellers with Symmetrical Sections at Zero Blade Angle," NACA TN-679, 1938.
- ² Gutin, L., "On the Sound Field of a Rotating Propeller," *Physikalische Zeitschrift der Sowjetunion*, Vol. 9, 1936, p. 57 (translated in NACA TN-1195, 1948).
- ³ Lowson, M. V., "Helicopter Noise: Analysis-Prediction and Methods of Prediction," *AGARD Lecture Series No. 63 on Helicopter Aerodynamics and Dynamics*, 1973.
- ⁴ Farassat, F., Nystrom, P. A., and Morris, C. E. K., Jr., "A Comparison of Linear Acoustic Theory with Experimental Noise Data for a Small-Scale Hovering Rotor," AIAA Paper 79-0608, Seattle, Wash., 1979.
- ⁵ Shenoy, K. R., "Semi-empirical High-Speed Rotor Noise Prediction Technique," *38th Annual National Forum of the American Helicopter Society*, Anaheim, Calif., 1982.
- ⁶ Schmits, F. H. and Boxwell, D. A., "In-flight Far-Field Measurement of Helicopter Impulsive Noise," *Journal of the American Helicopter Society*, Oct. 1976.
- ⁷ Boxwell, D. A., Yu, Y. H., and Schmits, F. H., "Hovering Impulsive Noise: Some Measured and Calculated

Results," NASA CP-2052, 1978 (also in *Vertica*, Vol. 3, No. 1, 1979).

- ⁸ Spletstoeser, W. R., Schults, K. J., Schmits, F. H., and Boxwell, D. A., "Model Rotor High-Speed Impulsive Noise — Parametric Variations and Full-Scale Comparisons," Paper 83-39-53, *39th Annual National Forum of the American Helicopter Society*, 1983.
- ⁹ Caradonna, F. X. and Isom, M. P., "Numerical Calculation of Unsteady Transonic Potential Flow over Helicopter Rotor Blades," *AIAA Journal*, Vol. 14, No. 4, Apr. 1976, pp. 482-488.
- ¹⁰ Hilton, W. F., "The Photography of Aircrew Sound Waves," *Proceedings of the Royal Society of London, Series A: Mathematical and Physical Sciences*, Vol. 169, 1938, p. 174.
- ¹¹ Tangler, J. L., "Schlieren and Noise Studies of Rotors in Forward Flight," Paper 77-33-05, *38th Annual National Forum of the American Helicopter Society*, Washington, D.C., 1977.
- ¹² Schmits, F. H. and Yu, Y. H., "Transonic Rotor Noise—Theoretical and Experimental Comparisons," *Vertica*, Vol. 5, 1982, pp. 55-74.
- ¹³ Ffowcs-Williams, J. E. and Hawkings, D. L., "Sound Generation by Turbulence and Surfaces in Arbitrary Motion," *Philosophical Transactions of the Royal Society of London, Series A: Mathematical and Physical Sciences*, Vol. 264, May 8, 1969, pp. 321-342.
- ¹⁴ Schmits, F. H. and Yu, Y. H., "Theoretical Modeling of High-Speed Helicopter Impulsive Noise," *Journal of the American Helicopter Society*, Jan. 1979.
- ¹⁵ Schmits, F. H. and Yu, Y. H., "Helicopter Impulsive Noise: Theoretical and Experimental Status," *International Symposium on Recent Advances in Aerodynamics and Aeroacoustics*, Stanford University, Stanford, Calif., Aug. 1983.
- ¹⁶ Yu, Y. H., Caradonna, F. X., and Schmits, F. H., "The Influence of the Transonic Potential Flow Field on High-Speed Helicopter Impulsive Noise," Paper 58, *4th European Rotorcraft and Powered Lift Aircraft Forum*, Italy, 1978.
- ¹⁷ George, A. R., "Helicopter Noise—State of the Art," AIAA Paper 77-1337, Atlanta, Ga., 1980.
- ¹⁸ Strawn, R. C., "Numerical Modeling of Rotor Flows with a Conservative Form of the Full-Potential Equations," AIAA Paper 86-079, 1986.
- ¹⁹ Chang, I-Chung, "Transonic Flow Analysis for Rotors, Part 2: Three-Dimensional, Unsteady, Full-Potential Calculation," NASA TP 2375, 1985.
- ²⁰ Pierce, A. D., *Acoustics*, McGraw-Hill Book Company, New York, N.Y., 1981, p. 180.
- ²¹ Rutherford, J. W., "The Aerodynamics and Acoustics of Rotating Transonic Disturbances," Ph.D. dissertation, Department of Aeronautics and Astronautics, Stanford University, Stanford, Calif., June 1986.
- ²² Holst, T. L. and Ballhaus, W. F., Jr., "Fast Conservative Schemes for the Full Potential Equation Applied to Transonic Flows," *AIAA Journal*, Vol. 17, Feb. 1979, pp. 145-152.
- ²³ Dougherty, F. C. et al., "TAIR-A Transonic Airfoil Analysis Computer Code," NASA TM-81296, 1981.
- ²⁴ Viviani, H., "Conservative Forms of Gas Dynamic Equations," *La Recherche Aerospaciale*, No. 1, Jan.-Feb. 1974, pp. 65-68.

- ²⁵ Hafez, M. M., Murman, E. M., and South, J. C., Jr., "Artificial Compressibility Methods for Numerical Solutions of Transonic Full Potential Equation," *AIAA Journal*, Vol. 17, Aug. 1979, pp. 838-844.
- ²⁶ Steger, J. L. and Caradonna, F. X., "A Conservative Implicit Finite Difference Algorithm for the Unsteady Transonic Full Potential Equation," *AIAA Paper 80-1368*, Snowmass, Colo., 1980.
- ²⁷ Chang, I-Chung, "Unsteady Transonic Flow Past Airfoils in Rigid Body Motion," Ph.D. dissertation, Courant Mathematics and Computing Laboratory, New York University, New York, N.Y., Mar. 1981.
- ²⁸ Zachmanoglou, E. C. and Thoe, D. W., *Introduction to Partial Differential Equations with Applications*, The Williams & Wilkins Company, Baltimore, Md., 1976, pp. 291-294.
- ²⁹ Strawn, R. C. and Tung, C., "The Prediction of Transonic Loading on Advancing Helicopter Rotors," *NASA TM-88238*, 1985.
- ³⁰ Purcell, T. W., "A Computational and Experimental Investigation of High-Speed Impulsive Noise from a Rotating Cylinder," *NASA TM to be published* 1987.
- ³¹ Caradonna, F. X. and Isom, M. P., "Numerical Calculation of Unsteady Transonic Potential Flow over Helicopter Rotor Blades," *AIAA Journal*, Vol. 14, Apr. 1979, pp. 428-488.

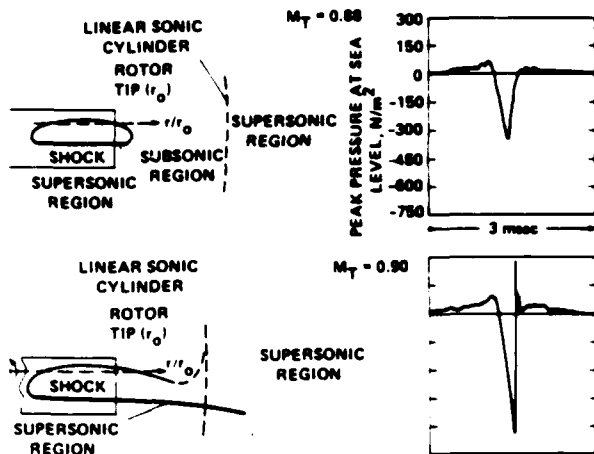


Fig. 1 Test data showing delocalization.

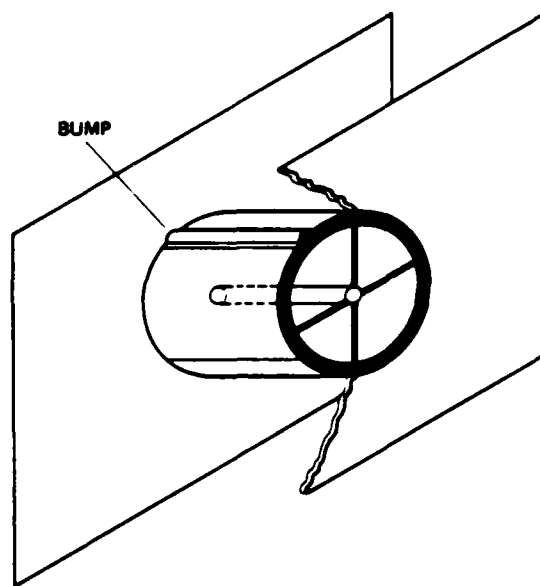


Fig. 3 Experimental configuration.

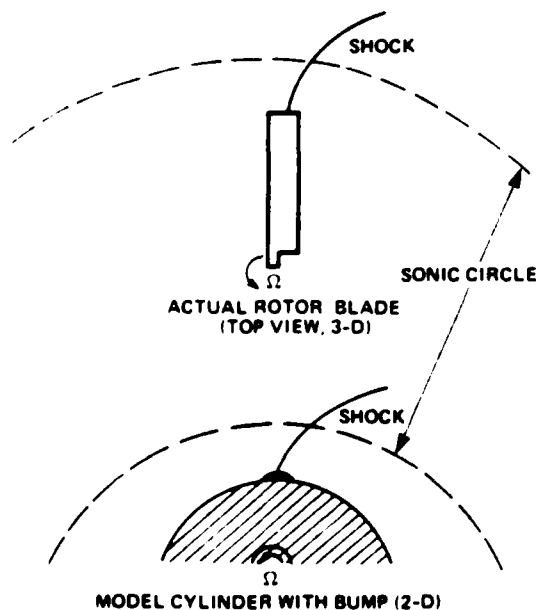


Fig. 2 Comparison of a rotor and the two-dimensional model.

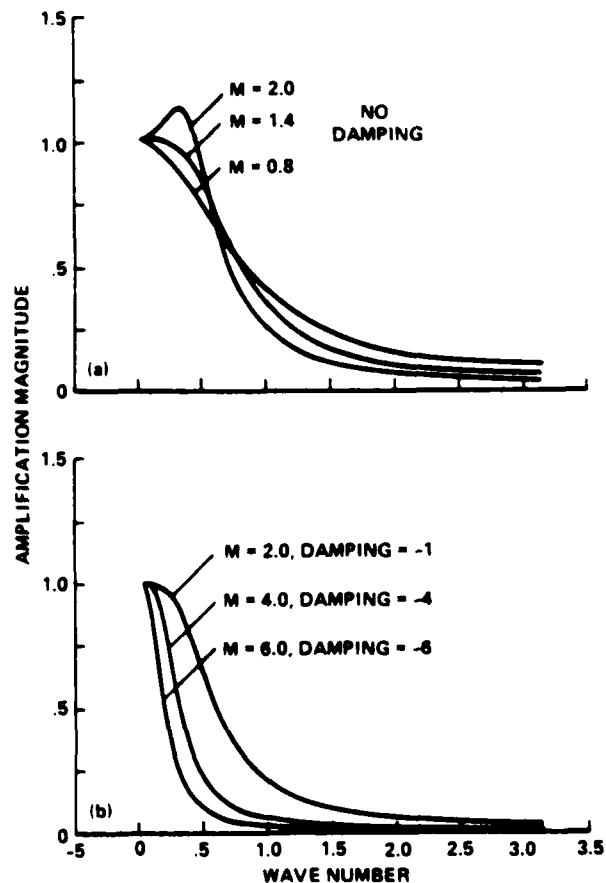


Fig. 4 Undamped and damped error amplification portraits.

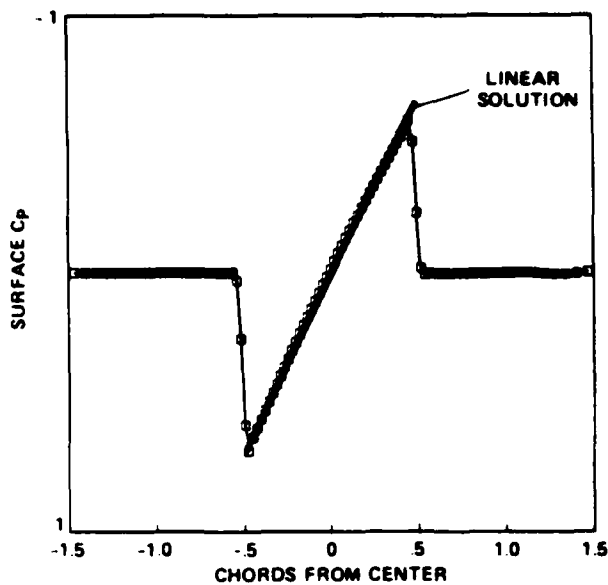


Fig. 5 Supersonic pressures for $M = 2.0$.

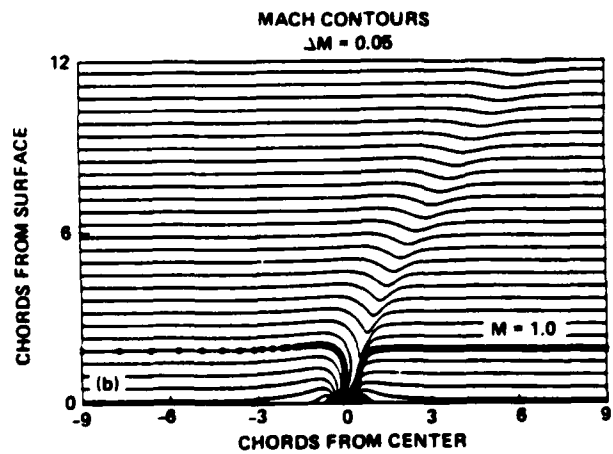
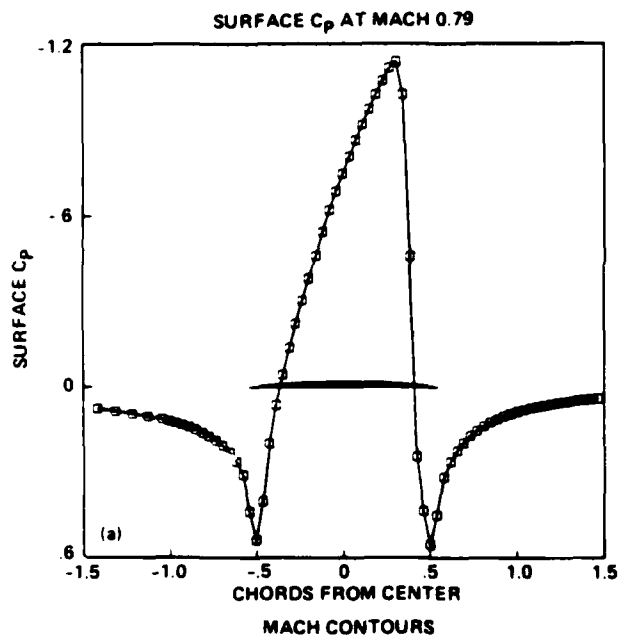


Fig. 6 Delocalized cylindrical case using a fine grid.

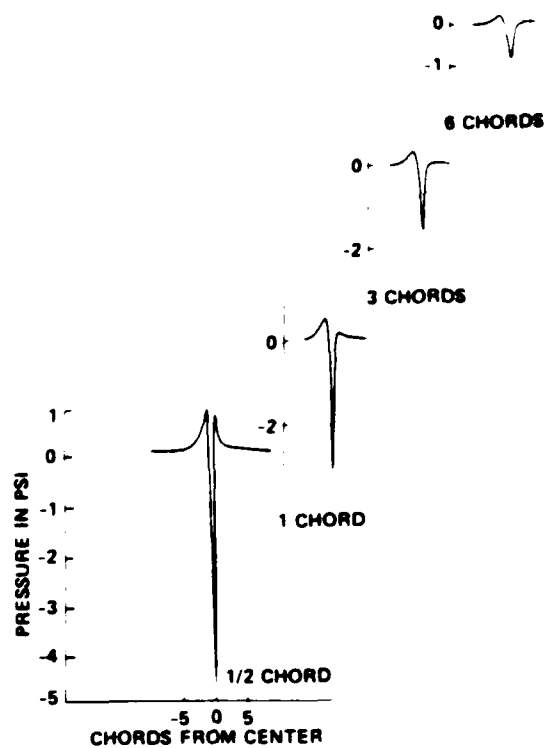


Fig. 7 Predicted experimental pressures.

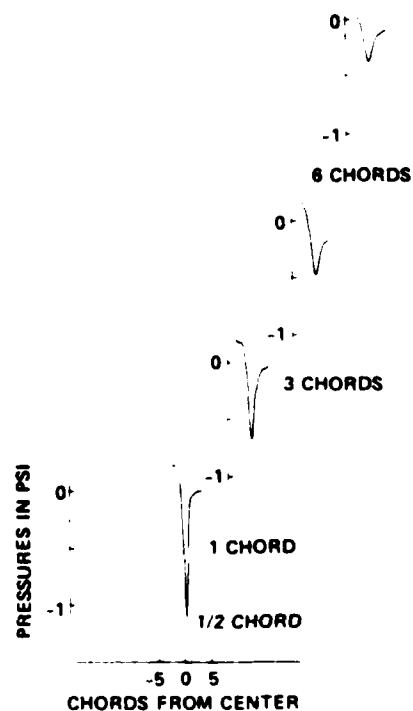


Fig. 8 Pressures as measured for all transducers.

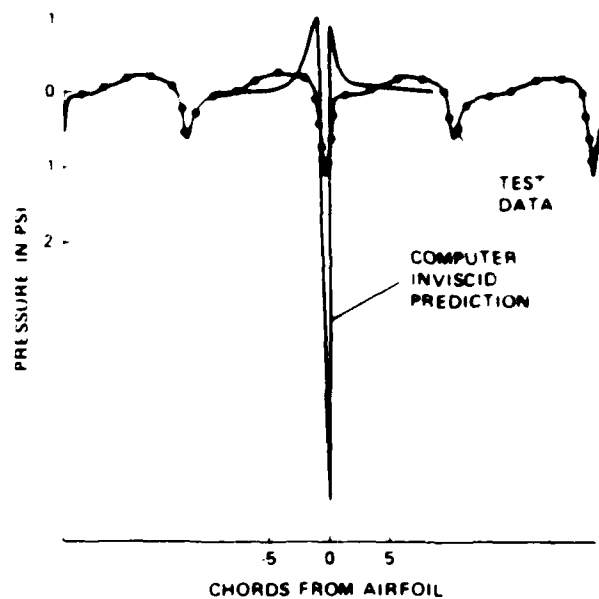


Fig. 9 Predicted and observed pressure pulses at the 0.5-chord location.

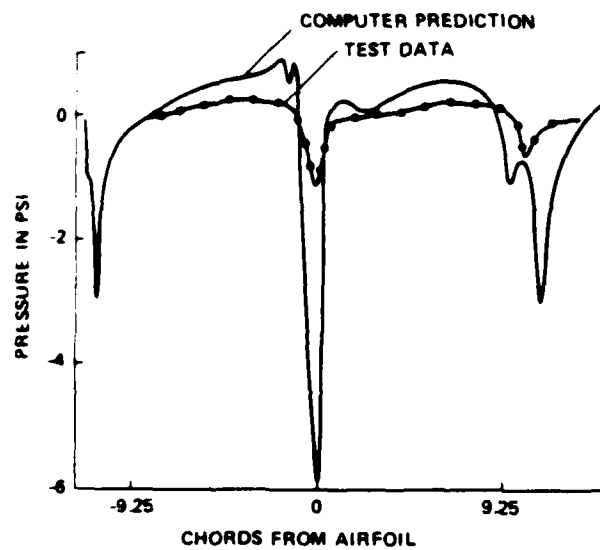


Fig. 10 Pressures at the 0.5-chord location using the modified cylinder shape.

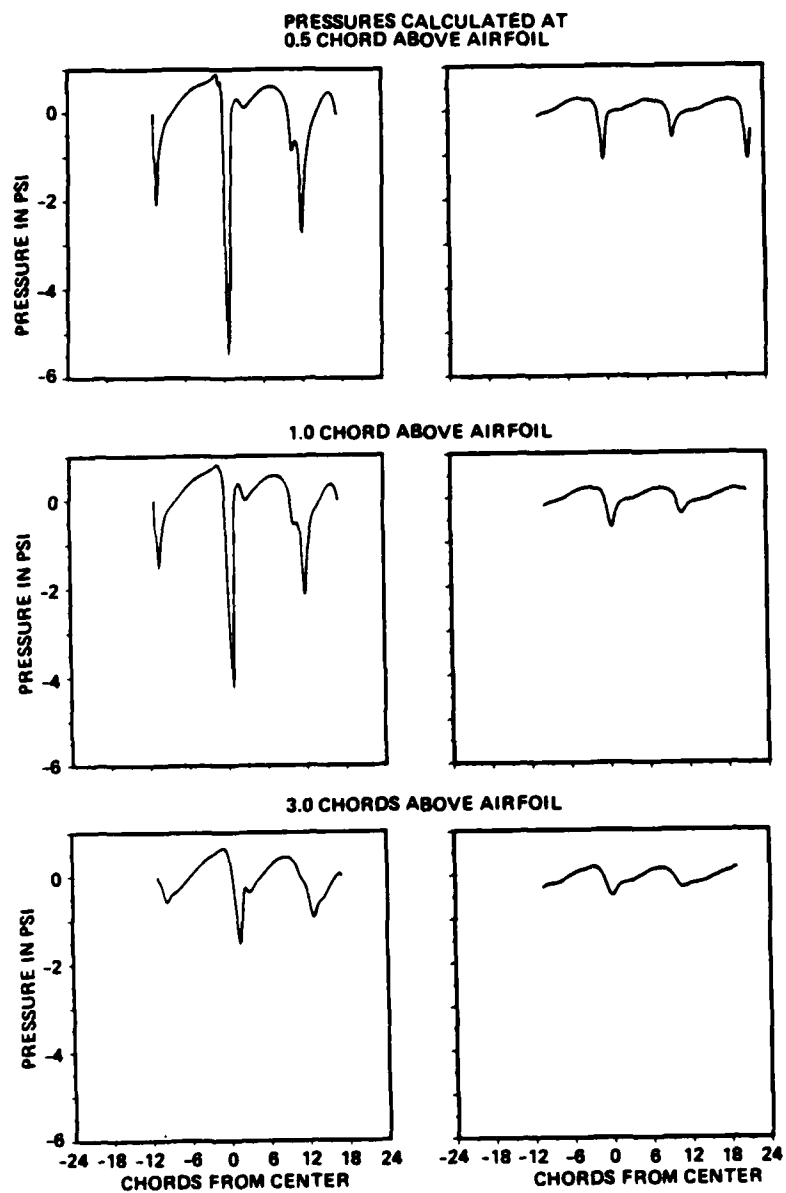


Fig. 11 Comparison of prediction and experiment.

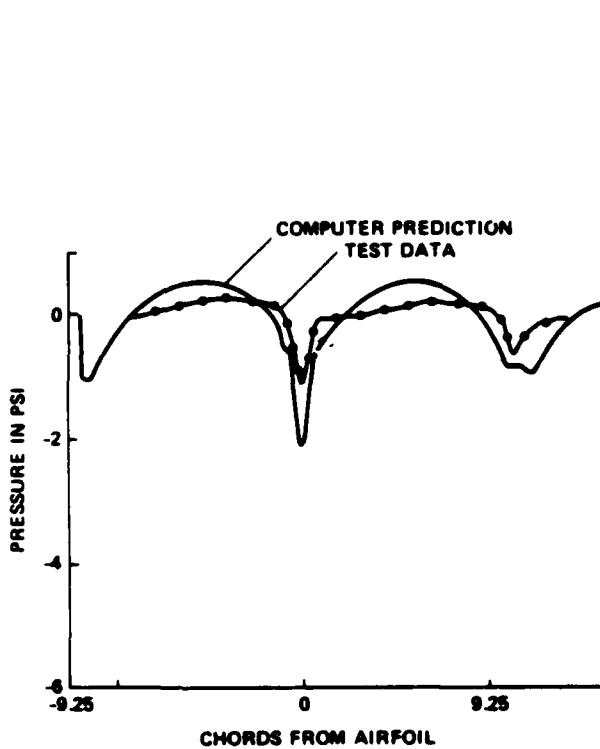


Fig. 12 Pressures from the fully corrected case.

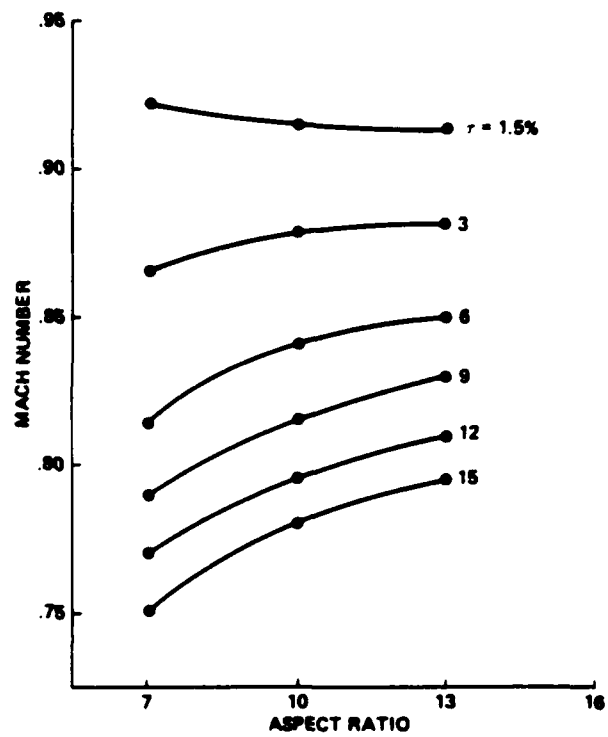


Fig. 13 Trends in the two-dimensional delocalisation Mach number.

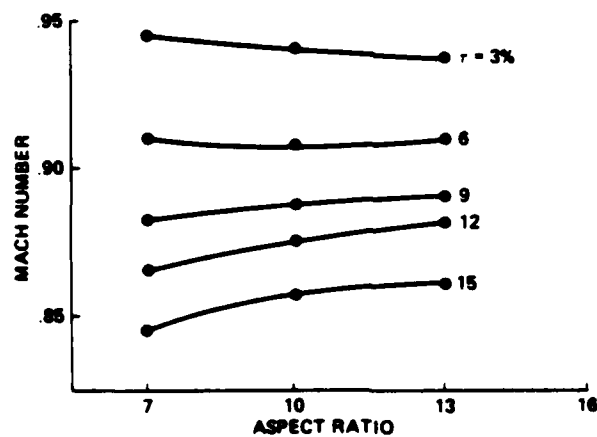


Fig. 14 Trends in the three-dimensional delocalisation Mach number.

END

4-87

DTIC